Master of Science Thesis

VT2013

The Alcyone CZT SPECT camera. Evaluation of performance using phantom measurement and Monte Carlo simulations

Erik Mattsson

Supervision

Jenny Oddstig, Cecilia Hindorf och Michael Ljungberg, Lund

This work has been conducted at

Department of Clinical Physiology, Skåne University Hospital, Lund

Department of Medical Radiation Physics,
Clinical Sciences, Lund
Lund University

Background Coronary artery disease is one of the most common causes of death. A common cardiac examination is to give a visualization of the myocardial blood flow by injecting a radio pharmaceutical and detect the radiation with a camera. The camera has for decades been using thallium doped sodium iodide (NaI(Tl)) as the detector material. New detector materials have been developed because of the physical limits of the NaI(Tl). The new clinically available material is cadmium-zinc-telluride. One manufacturer has placed 19 detector panels with pinhole collimators sharing a common focal point. This camera is relatively new on the market and not thoroughly investigated.

Purpose It has been investigated if the image quality could be improved with a narrower energy window, the sensitivity and spatial resolution within the field of view (FOV), whether the image was affected by different source locations was investigated. Finally the detection limit for heart defects in a physical phantom and in XCAT phantom was found.

Material & method A list mode acquisition was performed with a Data Spectrum phantom with a cardiac insert containing a basal defect, which simulated a myocardial infarction. The energy window was changed from ±10% to ±5% and the acquisition time was changed acquire the same statistics. The resolution was determined by fitting a Gaussian curve to a line source measurement. The detector specific sensitivity and the sensitivity in the reconstructed images were measured by using a spot marker at different positions. The positioning effect were investigated by placing the Data Spectrum phantom with a cardiac insert without any defects at different positions, the measurements were also performed on a patient. The defect limit was investigated by simulating defects with different positions and wall thickness in a voxel based, CT-scanned, anthropomorphic phantom and a XCAT phantom using a verified Monte Carlo software.

Results It was found that a reduction in energy window did not improve image quality and the acquisition time or activity had to be increased 25% in order to compensate of the loss of counts. The spatial resolution was unchanged over the investigated area. The detector specific sensitivity varied up to a factor 2 with the source position, but the sensitivity in the reconstructed images varied only 4%. A translation of 2 cm of the patient gives rise to positioning effect which are great enough to possibly change the diagnosis. The detection limit for defects in the anthropomorphic phantom was determined to be between 15% and 30% of the wall thickness. For the NaI(Tl) camera the detection limit have been found to be 50%. The detection limit for the XCAT phantom was not found.

[1] Department of clinical physiology and nuclear medicine, Skåne university hospital, Lund, Sweden

[2] Department of Medical Radiation Physics, IKVL, Lund University, Sweden

Svenskt populärvetenskalig sammanfattning

Hjärt- och kärlsjukdomar är en av vår tids största folksjukdomar. En undersökning för att studera blodflödets i hjärtats kranskärl är en så kallas myokardscintigrafi, där ett radioaktivt preparet injiceras i blodomloppet och en kamera detekterar den emitterade strålningen. Myokardscinitgrafi är den vanligaste typen av undersökning inom området nuklearmedicin och ger en relativ hög stråldos till patienten. Då undersökningen ger en hög stråldos är det önskvärt att minska stråldosen. Detta kan göras genom att öka kamerans kännslighet. En ökad kännslighet kan även användas till att förkorta undersökningstiden vilket gör att fler patienter kan undersökas. Under flera årtionden har materialet talliumdopad natriumjodid (NaI(Tl)) använts i kamerorna. På grund av fysikaliska begränsningar är det svårt att göra stora förbättringar med det detektormaterialet. Forskningsframsteg har gjort att halvledare tillverkade av kadmium-tellurid och zink-tellurid (CZT) blivit tillräcklig effektiva och billiga att använda inom sjukvården.

Till skillnad från NaI(Tl), som behöver PM-rör för att ge en elektrisk signal, ger CZT direkt en elektrisk signal när den utsätts för strålningen från en myokardscintigrafi. Förmågan att ge signal utan PM-rör gör att detektorn kan göras mycket mindre. En tillverkarare har använt denna egenskap för att skapa en kamera med flera detektorpaneler som samtidigt samlar in den emitterade strålningen från olika vinklar. Att det samlas in strålning från olika vinklar samtidigt gör systemet effektivt jämfört med NaI(Tl) kameror och insamlingstid eller administrerad aktivitet kan minskas.

Kameran är så pass ny att det finns egenskaper som inte helt undersökts. Några av dessa undersöktes i detta arbete. Systemets upplösning, hur stor en tunn linje avbildas, undersöktes och fanns variera väldigt lite över ett stort område. Den variationen som fanns kunde förklaras med en osäkerhet i beräkningen av upplösningen. Känsligheten för varje panel mättes upp då en punktkälla placerades på olika positioner. Det visade sig att känsligheten för individuella detektorer varierade kraftigt med källpositionen men att känsligheten efter det att 3D volymen beräknats var densamma för alla positioner, vilket tyder på att variationerna i känslighet för de olika detektorerna tar ut varandra i rekonstruktionen.

Detektorgeometrin i kameran gör att kameran har en begränsad mätvolym. Det undersöktes hur känsligt systemet var för positionerings effekter inom mätvolymen. Genom att placera ett fantom, en behållare som efterliknar en patient, optimalt i kameran och på ett par cm avstånd från den optimala positionen kunde det skapas bilder som visade positioneringseffekten. Det visade sig att det blev stor skillnad på resultatet vid en förflyttning på 2 cm. Eftersom fantomet är en förenkling av verkligheten och att det finns hjärt- och lungrörelser i en patient som kan överskugga effekterna i fantommätningen gjordes samma försök för en patient. Patientens bilder förändrades så pass mycket vid en liten förflyttning att det skulle kunna påverka diagnosen. Denna positioneringseffekt finns inte på NaI(Tl)-kameror.

Genom att använda ett beräkningsprogram, utvecklat vid institutionen för medicinsk strålningsfysik vid Lunds universitet, som beräknar hur kameran skulle mäta en källa undersöktes det hur olika stora hjärtdefekter kunde hittas med CZT-kameran och detta jämfördes med forskningsresultat från NaI(Tl)-kameran. En erfaren läkare kunde se en defekt som var 2 cm lång, täckte 60° av vänster hjärtkammare och var 30 % av hjärtmuskelns tjocklek. När defekten endast var 15 % av hjärtmuskelns tjocklek kunde defekten inte längre ses, därmed så är detektionsgränsen för CZT-kameran mellan 15 % och 30 % av hjärtmuskeln. För NaI(Tl)-kameror så har det visat sig vara svårt att finna defekter som är tunnare än halva muskeltjockleken. Det konstaterades också att defekter som var placerade mot bröstet var lättare att se än djupare belägna defekter.

Table of contents

Svenskt populärvetenskalig sammanfattning 1
Background 4
NaI(Tl) camera 4
CZT detector material 5
Energy tailing 5
Discovery NM 530c 7
Image reconstruction 8
AIM 11
Materials and Methods 12
Experimental studies 12
Monte Carlo simulations 13
Monte Carlo verification 14
The spatial resolution 14
The sensitivity 14
The image dependence on the energy window 15
The image dependence on the reconstruction parameters 15
The image dependence on the source location 16
The detectability of small lesions 16
Comparison: CZT camera versus NaI(Tl) scintillation camera 17
Results 18
Monte Carlo verification 18
The spatial resolution 20
The sensitivity 20
The image dependence on the energy window 21
The image dependence on the reconstruction parameters 22
The image dependence on the source location 24
The detectability of small lesions 25
Comparison: CZT camera versus NaI(Tl) scintillation camera 27
Discussion 28
Monte Carlo verification 28
The spatial resolution 28
The sensitivity 29
The image dependence on the energy window 29

The image dependence on the reconstruction parameters 30
The image dependence on the source location 30
The detectability of small lesions 31
Comparison: CZT camera versus NaI(Tl) scintillation camera 32
Conclusions 32
Acknowledgements 32
Appendix 1 33
References 34

Background

Myocardial perfusion imaging is the most common diagnostic procedure in nuclear medicine [1-3]. The procedure is often time consuming because it may require two acquisitions as one- or two days protocols and each acquisition is long compared to other procedures. Cardiac imaging is also an examination that gives a relatively high effective dose.

In cardiac imaging, a radiopharmaceutical is intravenously injected and the activity concentration taken up by the myocardium is large compared to the surrounding tissue, but there is also an increased uptake in the liver and in the intestines. The emitted gamma radiation is detected by an imaging device that produces a visual map of the activity distribution which is proportional to the myocardial blood flow. In order for the images to be useful a certain number of photons need to be registered. If the effective dose is to be reduced the administered activity has to be reduced and the acquisition time has to be longer to compensate.

Since the cardiac imaging procedure is a very common examination much attention has been focused on optimizing the equipment, the imaging procedure and reconstruction protocols. The most common imaging camera is the Anger scintillation camera with a NaI(Tl)-crystal. The areas where the NaI(Tl)-camera can be improved are limited with the current scintillation detector technology. Since there still is a need for further improvement in cardiac imaging improvements have been made in alternative detector material. An alternative detector material available at this time is Cadmium-Zinc-Telluride (CZT) detector. Cameras with the CZT material are currently available from two manufacturers. The cameras have recently been made available for clinical use and not every aspect of the cameras have been thoroughly investigated. The purpose of this work is to examine some of the properties of one of these commercial CZT cameras and to give a comparison to a camera with NaI(Tl)-crystal.

NaI(Tl) camera

The Anger scintillation camera is up to day the most commonly used camera for single photon emission computed tomography (SPECT). The camera uses a parallel-hole collimator to discriminate photons so that only those photons which impinge more or less orthogonally to the collimator surface will pass the collimator and reach the crystal. Most of the photons that strike the NaI(Tl)-crystal deposit all or part of its energy into the crystal. The energy is then transformed through de-excitations to visible scintillation photons but with a low intensity. The scintillation photons is collected by multiple photomultiplier tubes (PMT) where each of the PMT convert the scintillation light into a measurable electrical signal that is regarded to be proportional to the detected intensity of the scintillation light. The signals from all the PMTs that are triggered by a photon interaction are used to calculate the position of the primary photon interaction location. By using multiple PMT it is, from the centroid of the scintillation light, possible to determine the point of interaction on a smaller scale than the dimension of the PMT. The intrinsic spatial resolution of a NaI(Tl)-crystal is in the order of 3-5 mm but depends on the crystal properties and photon energy [5].

The indirect process of converting photon energy to an electrical signal via scintillation emission leads to a statistical error in the determination of the absorbed energy (i.e. a poor energy resolution). This is due to a low number of information carriers, free electrons, after the absorption of the scintillation photons. A poor energy resolution makes it hard to separate peaks in the pulse-height energy distribution. Furthermore, it will lead to photons that have been scattered in the patient to be

detected within the energy window. These events do not reflect the origin of the radionuclide emitting the photon since the direction has been changed in the phantom. A detector with good energy resolution minimizes this unwanted contribution of scatter in the image. The energy resolution of NaI(Tl) is in the order of 9-10% FWHM at 140 keV for modern crystals and is very difficult to improve. To improve energy resolution an alternative detector material is required.

CZT detector material

The CZT is a semiconductor material consisting for cadmium-telluride and zinc-telluride. The deposited energy from the photons is transferred to electrons by photo-interactions and the electrons then transfer the energy to secondary electrons which are excited form the valance band to the conduction band in the semiconductor material. The energy requirement to excite an electron to the conduction band depends on the material band gap. For CZT, the band gap ranges from 1.53 eV to 1.64 eV depending on the composition [6]. The band gap is large enough that there is low probability of thermal excitation to the conduction band at room temperature and the detector material is therefore usable without a cooling system. The excitation to the valance band creates an electron-hole pair. An electric field is applied over the semiconductor which causes the electrons in the valence band to move towards an array of anodes, where each anode can collects charges. In the CZT material, the drift velocity of the electrons is greater than the drift velocity of the holes. The signal is therefore extracted from the anode [6, 7]. Each of the anodes in a CZT camera represents a pixel in the image at the corresponding location. Therefore these types of detector system are sometimes called pixelated detectors. If the gap between the electrons is small and the same voltage is applied to all of the anodes the electric field is the same as if the anode was not pixelated [6].

The energy requirement to create an electron-hole par is approximately three times higher than the band gap, that is, around 4.6-5 eV, [1, 7, 8]. This energy requirement along with a Fano factor of 0.15 [1] results in a higher energy resolution than the NaI(Tl) material. The Fano factor is a value that correspond the lower observed variance compared to the Poisson variance because of the limited energy levels which the electrons can occupy in the material.

Energy tailing

The CZT semiconductor detector often consists of a solid block of CZT and small electrodes act as anode. This configuration allows charges to diffuse along the crystal and interact with more than one anode. This leads to an intrinsic spatial resolution that is larger than the detector size (i.e. pixel size).

During the movement of the electron cloud towards the anode the cloud will grow in size because of charge diffusion and charge repulsion [6]. When the electrons drift towards the anode a voltage change will occur and this change will be the extracted signal [9]. Because of the spatial distribution of the electron cloud there is a probability for the electron cloud to affect the field near two or more anode plates. All the affected pixels will share the total charge, but only one of pixels be register will a signal [1, 6]. If the initial interaction was located so that the entire electron cloud only affects one anode then that anodes response will only depend on the deposited energy and the depth-of-interaction [1, 6]. The fraction of shared event depends on the detector geometry and can be described by Equation 1 [9].

Equation 1

$$fraction\ of\ shared\ events = 1 - (a + 2c + 2r)^2/(a + g)^2$$

where *a* is the anode width, *g* is the anode spacing, *r* is the radius of the electron cloud and *c* is the collection width, which is $min(g/2, a/20)$.

Even if the entire electron cloud is collected by one of the anodes it is possible for the neighboring anodes to produce a signal provided that the signal collection time is shorter than the electron drift time. This effect is explained in the Schockley-Ramo theorem [6].

While the electron cloud drifts towards the anode some of the electrons will undergo trapping or recombination which results in a loss of signal [6]. Trapping is the phenomenon of an electron moving into an energy state of one of the impurities in the material, where the electron might be held for a sufficient amount of time that it does no longer contribute to the electron cloud [6]. Electrons and holes can spontaneously recombine, but it is most likely that recombination occur at impurities which attract both electrons and holes which recombine at the impurity [6]. Since the probability of trapping and recombination increases close to impurities the signal loss depends in the purity of the crystal.

The radius of the electron cloud and the drift time depend also on the depth-of-interaction in the crystal. A shallow interaction makes the diffusion time longer thereby cause a larger fraction of the electron to be lost and the longer diffusion time also cause the electron cloud to be laterally larger. Consequently, the probability that it produces a signal on more than one pixel decreases with the interaction depth. The signal reduction from the recombination, trapping and the charge sharing between pixels will result in a tail in the pulse-height distribution located on the lower side of the location for the photopeak, as can be seen in Figure 1. A comparison between the energy spectrum acquired from $^{99}Tc^{m}$ with a NaI(Tl)-detector and a CZT detector can be seen in the illustration in Figure 2. Here, the comparison shows that the improved energy resolution is somewhat reduced because of the energy tailing.

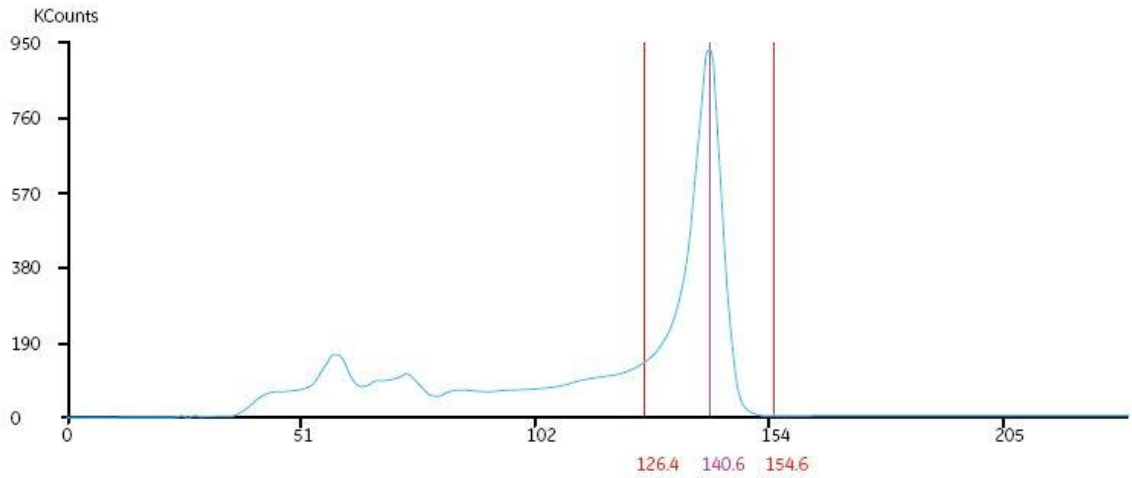

Figure 1: Tc-99m spectrum acquired with the GE Discovery NM 530c system [10]

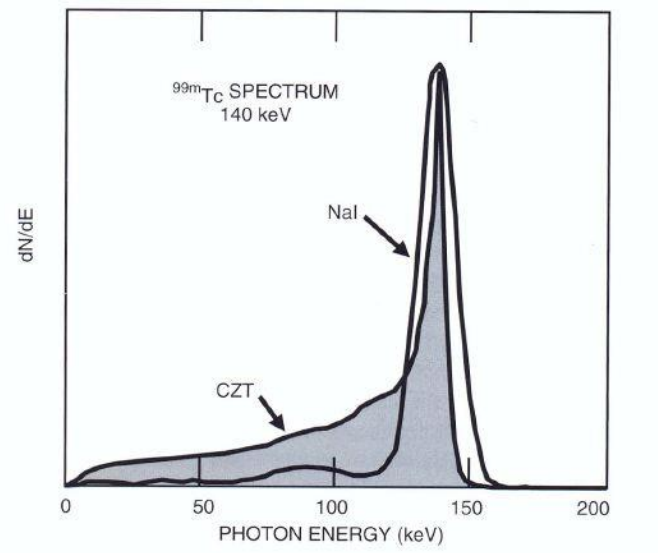

Figure 2: Illustration of ^{99m}Tc spectrum from CZT and NaI detector [1]

Discovery NM 530c

The Discovery NM 530c system (General Electric, Wisconsin) has 19 panels of CZT detectors [2, 3, 10]. Each panel has a separate pinhole collimator which is used in a geometry which reduces the projection size of the object on the detector surface, described in Figure 3 [10]. The high intrinsic spatial resolution makes it possible to have small detector panels while maintaining acceptable sensitivity. Each of the detector panels has the dimension 8 x 8 cm and each consists of four modules with the dimension 4 x 4 cm. Each panel has 32 x 32 pixels with the dimensions 2.46 x 2.46 mm^2 [3, 10]. A photography of a module is in figure 4.

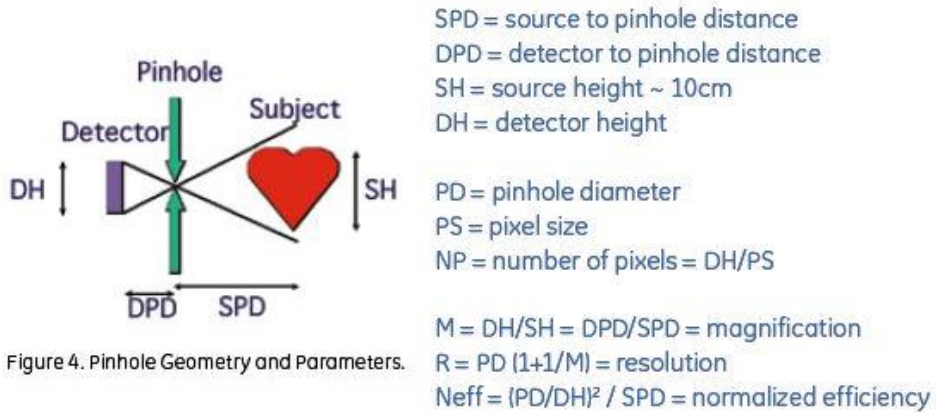

Figure 3: Detector and pinhole collimator geometry, image from GE white paper [10]

The detectors are placed in three rows with the outer rows containing fewer panels than the middle row, se Figure 5. The pinhole collimators of all the detectors are aligned so that they share a common focus point, the shared focal point gives the detectors an overlapping field of view which makes it possible to acquire simultaneous measurements of an object from several different projection angles [2, 10]. The effective Field Of View (FOV) is defined by a sphere with a diameter of ~19 cm. Within the virtual sphere the sensitivity varies because of the pinhole collimators [2]. This variant sensitivity leads to a reduction in the detected count rate of photons emitted from nearby organs because these are located further away from the focal point [11]. While each of the detectors does not have a higher efficiency than the previously used NaI(Tl) detector the ability to acquire simultaneous

projections greatly increase the system efficiency. Each pixel has a separate electronic processing unit which greatly reduce the dead time at high count rates [12]. The detector dead time reduce the efficiency of the system [6]. At the commissioning of the system a linear count rate was measured well above the maximal used activity so the dead time does not greatly impact the count rate.

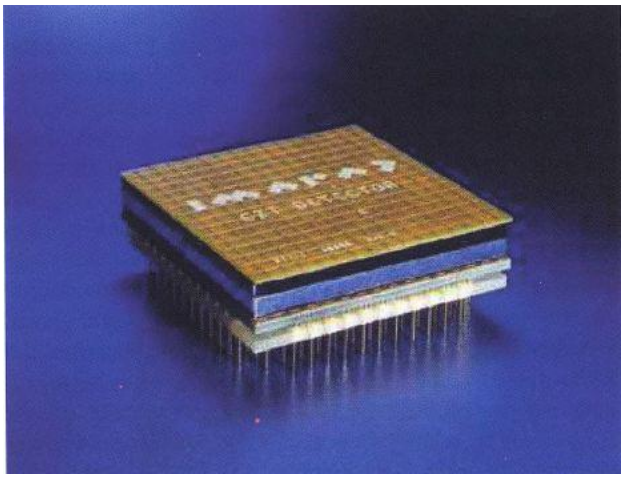

Figure 4: An Imarad CZT module with 256 pixels [1]

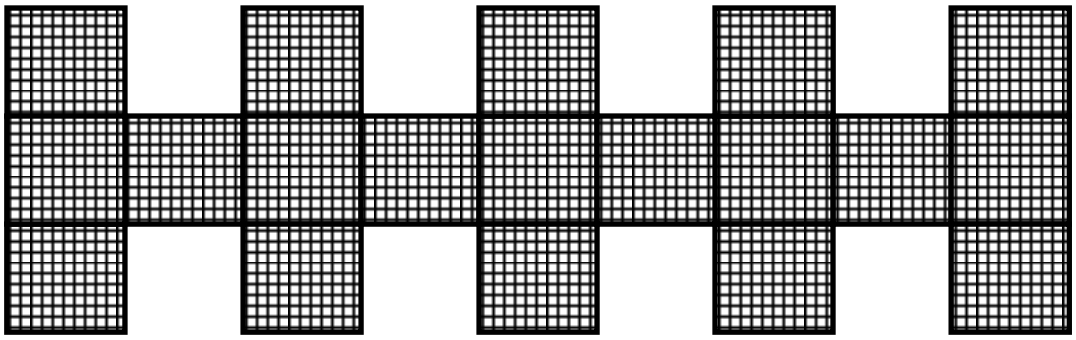

Figure 5: Conceptual description of the detector array in the Discovery NM 530c

Image reconstruction

Tomographic reconstruction was made in the clinical workstation Xeleris (General Electric Helthcare, Milwaukee,Wi) by the use of the systems reconstruction software. Due to commercial restriction the details of the actual procedure are somewhat limited. Reconstruction is performed with a maximum-likelihood expectation-maximization (ML-EM) reconstruction algorithm with a Green One-Step-Late (OSL) correction [3, 13, 14]. In the ML-EM reconstruction algorithm, the most likely activity distribution is calculated via an iterative “estimate, compare and update” procedure. The first step is an initial estimate of the activity distribution and this estimate is usually set to a uniform distribution. Then in a projector step, a calculation of a projection is made of how each of the detectors would measure the estimated activity distribution. This requires knowledge of the detector geometry and sensitivity of each part of the detector system. A comparison is then made between the calculated projections and the measured projection resulting in an error projection for each detector panel. The error projection is then back-projected into the image volume and the resultant error image is used in a multiplication to update estimated activity distribution. The underlying assumption is that as the

error projection converges to unity the estimated activity distribution converges to the true distribution. In each iteration areas where the proposed distribution differs a lot from the true distribution will be changes more than areas where the estimation is closer to the true distribution [15]. The estimate will converge with the true distribution with increased number of interactions, with the coarse structures converging at less iteration than the details. A schematic view of the reconstruction is found in Figure 6.

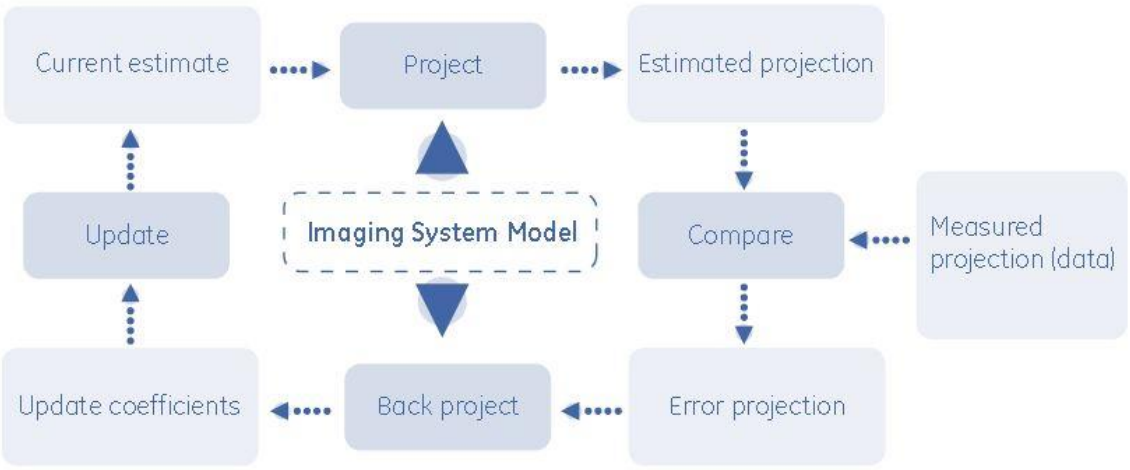

Figure 6: Schematic description of the MLEM reconstruction algorithm [10]

When the number of iterations increases so does the image variance, which is a measure of the image noise. The ML-EM suffers from a trade-off between convergence and noise [15]. The increased noise level is somewhat suppressed due to the post reconstruction filtering.

The OSL correction determines the image "smoothness" in the reconstruction process and represses the noise. The OSL algorithm come with two variables for the user specify, α and β. The values for α and β that produces the best image depends on the distribution in the image and viewer preferences.

Image post processing is performed on each of the reconstructed slices with a Butterworth filter. The magnitude of the Butterworth filter as function of the frequency ω is calculated by Equation 2

Equation 2

$$|M|^2 = \frac{1}{1 + \left(\frac{\omega}{\omega_0}\right)^{2n}}$$

ω_0 is the cut-off frequency and n is the power and determine the slope of the filter. A small change in the cut-off frequency can dramatically change the final image.

Although each image set got a separate set of optimal reconstruction parameters it is not viable to optimize each image. Each clinic determines a set of parameter which produces an acceptable image quality for all patients. At the Department of clinical Physiology and nuclear medicine at Skåne university hospital in Lund, Sweden, a separate set of reconstruction parameters is used for gated and ungated images as well as for rest and stress images. The parameters can be found in Table 1.

Table 1: Clinically used reconstruction parameter at SUS Lund [13].

	MLEM	Green OSL regularization		Butterworth post filter	
	Iterations	α	β	ω	n
Stress gated	40	0.51	0.3	0.40	10
Stress ungated	40	0.51	0.3	0.37	7
Rest gated	50	0.41	0.2	0.37	7
Rest ungated	50	0.41	0.2	0.37	7

AIM

The aims of this master thesis are the following:

- Investigate how the sensitivity and spatial resolution varies within the field of view
- Investigate the effect of the energy window on the image
- Evaluate how altering different reconstruction parameters alters the image
- Investigate how the source positioning affects the image
- Verify the SIMIND Monte Carlo software for Discovery NM 530c
- Determine the detection limit for defect thickness using phantom measurements and Monte Carlo simulations.

Materials and Methods

The investigation of the CZT-camera has been made using both experimental data from phantom measurements and data from real patient studies but also from data obtained by Monte Carlo simulations. The simulation package SIMIND is currently under development for simulation of solid state detectors as a parallel project [17]. All of the programming and simulation with the SIMIND software were performed by Dr Ljungberg. The DICOM files produced by software were imported into the database and thereafter treated as if they were acquired on the real CZT camera.

Experimental studies

The study in this thesis has been made using various sources and phantoms. These are described in the following text.

For point source measurements a spot marker from Eckert & Ziegler Isotope Products (No. SM-057-100U) were used [16]. The material and dimensions of the spot marker can be seen in Figure 7.

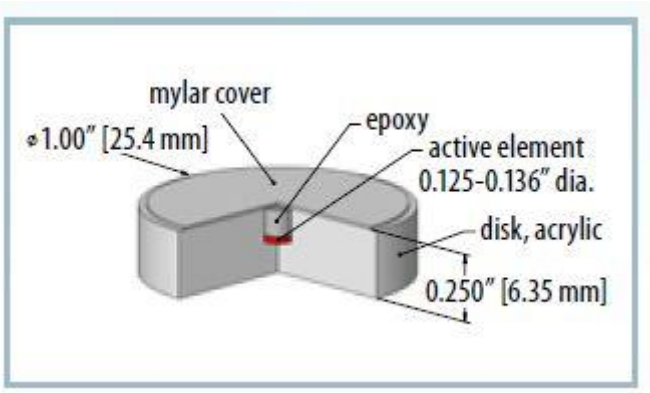

Figure 7: Illustration of a SM-057-100U spot marker from Eckert & Ziegler isotope products product catalog [16].

A line source was created by attaching polythene tubing to a ruler. Two dimensions of tubing were used, inner diameter of 0.60 mm and 0.86 mm and an outer diameter of 0.7 mm and 1.27 mm respectively. The tubings were filled with $^{99}Tc^{m}$ with an activity concentration of 58 MBq/ml and sealed with hypodermic needles syringe stoppers, se Figure 8.

Figure 8: Line source created with plastic ruler, plastic tubing and hypodermic needles, filled with $^{99}Tc^{m}$ solution

The physical phantom used was an elliptical anthropomorphic phantom with a cardiac insert and a spine-lung insert (Data Spectrum Corporation, Durham NC), Figure 9. The Cardiac Insert comes with the option to insert solid or fillable defects into the myocardium. The lungs were filled with a mixture of cork chippings and water.

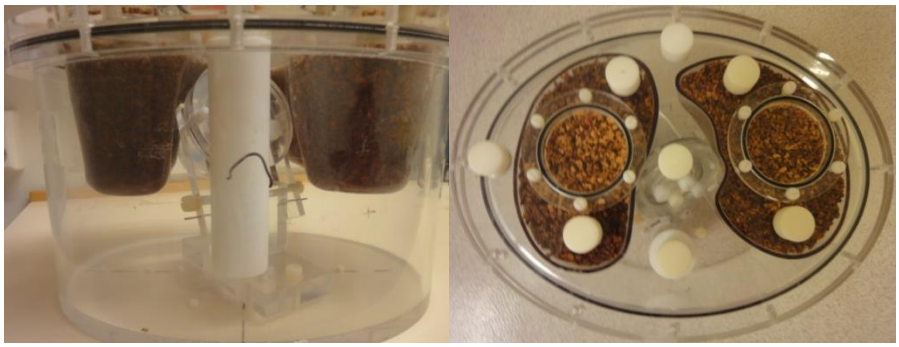

Figure 9: Elliptical anthropomorphic phantom with lung-spine insert and cardiac insert from Data Spectrum. Lungs filled with water and cork chippings.

Monte Carlo simulations

SIMIND is a Monte Carlo simulation software that is developed at the Daprtment of Medical Radiation Physics, Lund University [17]. Using information about the activity distribution and the density of an object the program statistically calculates how the radiation is detected, given a certain detector configuration. The geometry of the Discovery 530c NM has been provided Michael Ljungberg by General Electric as a non-disclosure agreement and therefore the simulated system compare well with the physical system.

As described earlier, a fraction depending on the depth of interaction of the electrons in the cloud may be lost due to physical processes. The SIMIND program does not explicitly simulate the recombination and trapping, but instead utilizes the Hecht equation, described in Appendix 1.

The Data Spectrum phantom, described above, was given available to us as digital voxel based phantom with heart, lungs, spine and two heart defects (courtesy of Dr Maria Holstensson, medical physicist at Huddinge Hospital, Sweden) defined by unique voxel codes in the images. The phantom matrix was originally 512 slices with the dimension 1024x1024. The phantom was centered in the middle of the matrix with a lot of air margin. The matrix was therefore rebinned in order to reduce the matrix size. The rebinning was used without interpolation in order to maintain the voxel codes. The final matrix had the dimensions 384x304 with 1 mm pixel size and contained 423 slices with 0.5 mm thickness. The modification of the matrices was done by a program written in IDL 8.2 (Exelis Visual Information Solutions, Boulder,CO).

To make the simulations more flexible, a computer routine based on the cardiac insert instead of the cardiac definition by the voxel codes, as described above, were used. This was done in order to be more flexible in the definition of defects. The analytical cardiac insert mimicked the real insert by consisting of a half sphere connected to a cylinder. The dimensions and the size of the ventricle were defined to exactly match the real insert. In the SIMIND code a polar and azimuthal angle assured a realistic alignment of the cardiac.

One of the more advanced digital phantoms available for the research community is the 4D extended Cardiac-Torso (XCAT) phantom [18]. The XCAT phantom is a NURBS based phantom which emulates cardiac and respiratory movement with a 4D positioning of the NURBS control points. In order to use the phantom in the SIMIND software the phantom needs to be voxelized, this is done through sampling the XCAT phantom with the desired voxel size.

Monte Carlo verification

One part of the verification was to compare the sensitivity of the Discovery NM 530c with the apparent sensitivity of the simulation software. Measurements were performed with a spot marker at seven positions within the field of view. The positions were the focal point and 2 cm along the vertical, longitudinal and lateral axis. Simulations were performed for the same positions. The ratio between the measured and simulated sensitivity were calculated.

Another step to validate the simulation software was a comparison between phantom measurements and simulations. The measurements were performed with the Data Spectrum phantom. The cardiac insert was used without any of the lesion inserts. The myocardial wall of the phantom was filled with an activity concentration of $^{99}Tc^{m}$ that corresponds to the concentration of the myocardium when a 70 kg patient is injected with a dosage of 2.5 MBq/kg and the assumed uptake fraction is 2% which results in 0.025 MBq/ml. The optional lung and spine inserts were not used and the phantom was completely filled with water. No background activity was used. Measurements were done with the heart in the center of FOV, 2 cm below and 2 cm along both direction of the longitudinal axis. The translation was done by moving the couch.

The criteria which the images were compared with were the defect appearance and position, the attenuation effects and the heart volume.

The spatial resolution

In order to evaluate how the spatial resolution varies within the FOV of the system line source measurements were performed. Measurements on the line sources were made with the line placed along the central axis of the camera and 2 cm along each direction along the vertical and lateral axis. The reconstructed images were evaluated in the software Amide 1.0.4. A Gaussian curve was fit to the apparent activity distribution at the middle of the line source and near each endpoint of the line source in the coronar slice that went through the line profile and the full width at half maximum (FWHM)of the fit was taken as the spatial resolution.

The sensitivity

Because of the use of pinhole collimators there is a geometric dependence on the sensitivity within the FOV. Several measurements were performed and the sensitivity was calculated for each detector for each of the source locations. To verify that the simulation software has an apparent sensitivity comparable to the measurements simulations were performed as well. The measurements and simulations were performed with the spot marker described earlier.

The measurement points were the focal point and 2 cm in each direction along the longitudinal axis, the vertical axis and the lateral axis. The translation of the source was achieved by moving the couch along longitudinal and vertical axes and by moving the source according to a paper with a mm grid which was aligned with the central axis. Once all the measurements were done tomographic reconstructions were performed and the actual positions of the source were estimated.

Once the source positions were known a simulation was made for each of the seven positions. The total number of counts in the source projection was extracted from the measurements and the simulation for each location and detector. Regions of interest (ROI) were used to select the point source projections and to avoid the background noises. The ratio between the measured and the

simulated mean counts were calculated for each source position and detector. The mean ratio and the standard deviation were calculated for each position.

The systemic sensitivity for obtained from reconstructed images was evaluated by calculating the sum of counts in all slices containing the point source. The sensitivity was calculated for each source position and normalized to the sensitivity in the focus.

The image dependence on the energy window

The CZT crystal has a better energy resolution than the NaI(Tl) crystal, but the pulse-height distribution shows a low energy tail that comes from a number of different physical processes. Some of scattered photons that make it past the pinhole collimator have energies high enough to give an additional contribution to the spectrum in the tail region. While it is possible in a simulation to differentiate events in this region apart from another it is impossible in a measurement to be able to measure the fraction of the tail that originated from scattered photons and the part that comes from charge sharing, recombination etc. In order to study the effect the energy window has on the image acquisitions with different energy window settings were obtained using list mode acquisition of a phantom with a myocardial defect. The acquisition was obtained with an energy window of ±10% and the acquisition time was altered to achieve a mean count comparable to a clinical stress image. The second energy window was set to ±5% and the acquisition time was changed to compensate for the loss of counts. Tomographic reconstruction was performed on the two data sets with the same reconstruction parameters and the image volumes were visually compared. The contrast between the defect and the healthy myocardium was calculated for each energy window setting using contrast equation, Equation 3

Equation 3

$$C = \left| \frac{\overline{count_{healthy}} - \overline{count_{defect}}}{\overline{count_{healthy}}} \right|$$

where *C* is the contrast, $\overline{count_{healthy}}$ is the average counts in a circular ROI in the healthy myocardium and $\overline{count_{defect}}$ is the average counts in a circular ROI in the defect. The ROI in the myocardium were placed in middle of the myocardium and the size was chosen so there was little of the spill out effect in the pixels in the ROI. The ROI in the defect were the same size as the myocardial ROI and was placed so that the middle of the ROI was placed approximately in the middle of the defect. There was some spill in effects in the defect ROI due to the reconstruction.

The image dependence on the reconstruction parameters

Knowledge in how each reconstruction parameter affects the final image is required in order to be able to choose reconstruction parameters which result in an improved image. While there is an interplay effect between the different parameters it is important to evaluate how each of the parameters affects the image separately.

Three series of reconstructions were performed where each had a different variable reconstruction parameter i) number of ML-EM iterations performed, ii) α and β in the OSL regularization and iii) the cut-off frequency for the Butterworth filter. The range of the parameters was chosen so that the values ranged outside the recommended clinical settings.

The reconstructions were performed on the stress acquisition from a patient, which had given a written consent that the patient material could be used for research.

Phantom studies were performed to find sets of reconstruction parameters which gave an increased contrast between a defect and the healthy myocardium and gave a lesser apparent thickening of the ventricle walls. The optimal sets of parameters were then applied to the raw data from a patient acquisition. The resulting images were presented to a physician with long experience of evaluation of cardiac imaging.

The image dependence on the source location

Because there are multiple pinhole collimators that share a common focal point a positioning dependence arises that is not present in the Anger scintillation cameras as long as the object being imaged is fully within FOV of the camera head. For various reasons the patient may be intentionally or not intentionally placed in the FOV in a sub-optimal way. It is therefore of importance to determine if and if so in what way the image is affected by a mispositioning of the patient.

In order to study the positioning effect, the Data Spectrum phantom with a cardiac insert filled with $^{99}Tc^{m}$ activity only in the myocardial compartment was used. The activity concentration used was 0.025 MBq/ml which corresponds to the myocardial activity concentration of a given dose of 2.5 MBq/kg assuming an uptake of 2% of the administered activity. The optional lung and spine insert was not used in these measurements.

An acquisition was performed with the phantom placed so that the focal point was a close to the center of the ventricle as possible. The phantom was then moved 2 cm in posterior, cranial and caudal direction, respectively, relative to the first measurement.

In a patient there is a non-uniform activity distribution, variable wall thickness, background activity and heart motion during the measurement. These effects may have a greater effect on the image compared to the positioning effects. Acquisitions for a patient at different positions were performed. An acquisition with optimal positioning and two acquisitions with sub optimal positioning were performed. The patient was moved 2 cm posterior and 2 cm cranial in the sub optimal acquisitions.

The detectability of small lesions

In order to evaluate the detectability of the CZT system myocardial perfusion simulations were conducted using defects of various thicknesses ranging from 25% to 100% transgression in steps of 25%. Simulations were made for both the Data Spectrum phantom and the XCAT anthropomorphic computer phantom where the latter phantom included cardiac motion.

For the Data Spectrum simulation a corresponding measurement of the physical phantom was made. A solid plastic defect that covered 60° of the myocardium, 100% of the wall thickness and 2 cm along the heart long axis was placed so that the defect edge was 6 mm from the heart base in the inferior position. In this measurement the lung-spine insert was used in the phantom. The myocardium was filled with a $^{99}Tc^{m}$ activity concentration of 0.41 MBq/ml. The phantom was a placed in the camera so that the focus point was as close to the middle of the cavity as possible and measurement with an acquisition time of 10 minutes, which result in better statistics than necessary, and an energy window of ±7.5 % centered at 140.5 keV was performed. The measurement was acquired in list mode and was altered so that the apparent acquisition times were long as it was needed, with the

given activity concentration, to achieve a mean pixel value comparable to the clinical images for a stress and a rest acquisition. The images were evaluated by a physician with long clinical experience.

Comparison: CZT camera versus NaI(Tl) scintillation camera

To compare the image quality between a CZT system and a NaI(Tl) scintillation camera a simulation study were made for a GE Ventri system. This dedicated cardiac SPECT system consists of a 18.5 cm x 36.5 cm NaI(Tl) crystal of thickness 0.952 cm equipped with a LEHR parallel-hole collimator. The energy resolution is 9.5% FWHM at 140 keV and an energy window of 20% is used. Sixty projections of size 64x64 (pixel size 0.64 cm) is routinely used. The radius of rotation is 25 cm. The SIMIND system have been verified in a doctoral thesis [19]

The simulation was performed with the Data Spectrum phantom with a cardiac insert and a lung insert. The cardiac insert was used without any defect and with an inferior basal defect with 15%, 30%, 45% and 100% of the heart wall thickness. The simulations with the NaI(Tl) camera were compared with simulations with the CZT camera for the same defects.

Results

Monte Carlo verification

The data for comparison between a simulated and measured point source for different positions has been evaluated for each position separately and independent on position. The mean ratio and the standard deviation in ratio for each position can be found in Table 2. The ratio for the entire system was 1.19±0.417. The range of the ratio for individual detectors was 0.88 to 5.24. With the exception of the 5.24 the highest ratio was 2.28. The ratio 5.24 comes from detector panel 17 with the source position caudal of the focal point. All projections were circular or slightly elliptical, except for the projection on before mentioned panel, which had an irregular shape. The simulated projection for this panel and position was circular. The projection 17 for the focus position and the caudal position can be seen in Figure 10.

Table 2: Mean ratio between the simulated and measured data for the seven positions. The distance between each measurement point was 2 cm.

Position	Ratio
Focus	0.98 ± 0.15
Anterior	1.09 ± 0.47
Posterior	0.97 ± 0.19
Cranial	1.06 ± 0.24
Caudal	1.21 ± 0.82
Sinister	0.99 ± 0.24
Dexter	1.13 ± 0.46

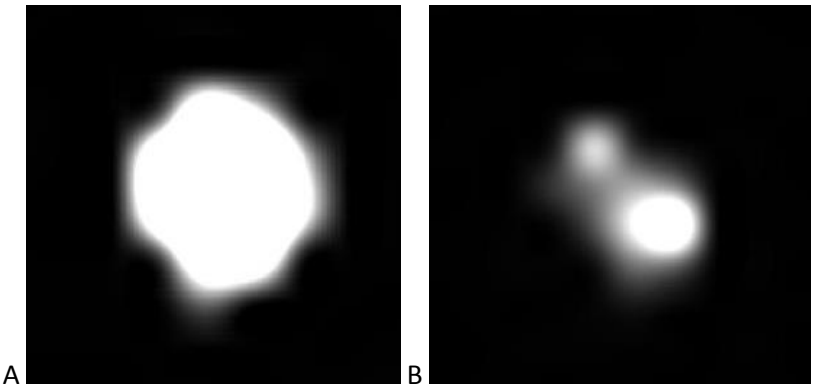

Figure 10: Projection 17 of the point source placed in focus (A) and 2 cm caudal (B).

The measurement and simulation of the Data Spectrum phantom with a defect was compared on several factors. The shape and size of the heart was considered as acceptable. It was not possible to achieve an exact match between the heart sizes because of the difficulties with the automatic segmentation. The visual comparison between the activity distributions was done in both slices along the three heart axes, Figure 11, and in polar plots, Figure 12. The SIMIND software produced simulated images both with and without attenuation within in the phantom, which can be seen in Figure 13. The calculation of the attenuation was evaluated as plausible when comparing the attenuation in the measurement and the simulation in Figure 12. The defect was found to be marginally larger in the measurement compared to the simulation, but it was found to be an acceptable difference.

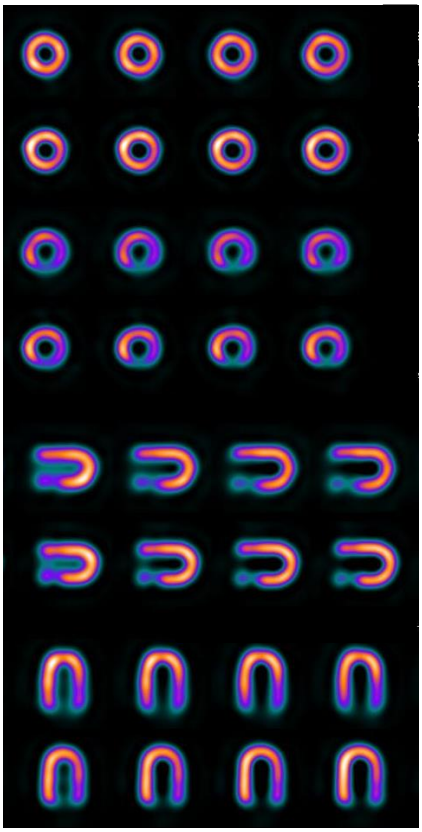

Figure 11: Short axis, vertical long axis and horizontal long axis slices of the Data Spectrum phantom as measurement (upper rows) and simulation (lower rows).

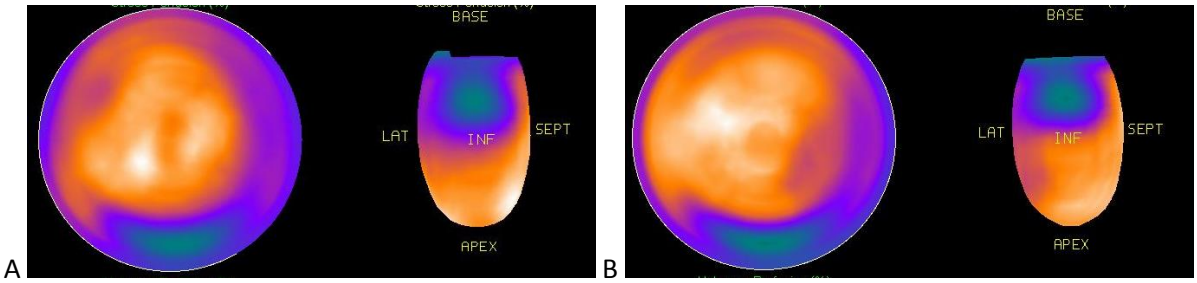

Figure 12: Polar plot and ventricle wall projection of the Data Spectrum phantom with a 100% 60° inferior defect as measurement (A) and simulation (B).

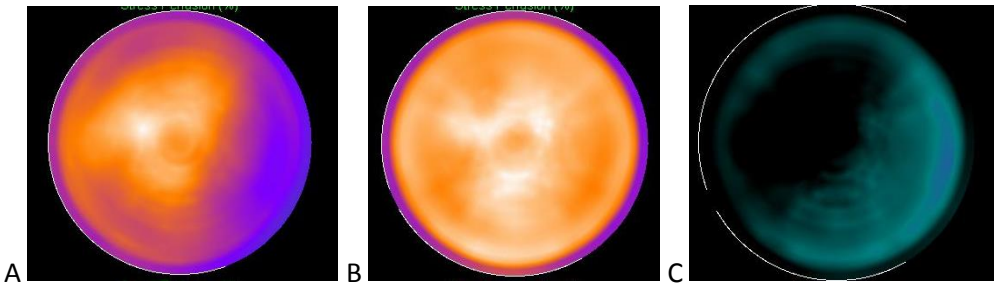

Figure 13: Simulated Data Spectrum phantom without defect with attenuation (A), without attenuation (B) and the difference between the polar plots (C).

The spatial resolution

The FWHM for the Gaussian profile at three positions for two measured line sources can be found in Table 3. The FWHM of the Guassian profiles ranges from 4.7 mm to 6.7 mm with a mean value of 5.8 mm.

Table 3: FWHM in mm for a Gaussian profile at three positions for two different line sources places at different positions. The distance between the source locations were 2 cm and the distance between the measurement points were 8 cm

[mm]	Line source position				
	Focus	**Anterior**	**Posterior**	**Sinister**	**Dexter**
Profile position	Line source 0.60 mm				
Cranial	5.5	5.4	6.7	5.8	5.6
Central plane	6.3	5.0	6.4	6.0	5.6
Caudal	6.0	5.3	6.2	5.6	5.6
	Line source 0.86 mm				
Cranial	5.8	4.9	6.1	5.9	5.6
Central plane	6.2	4.7	6.2	6.0	5.6
Caudal	5.6	5.1	6.3	6.0	5.9

The sensitivity

The measured sensitivity for each detector panel for seven source positions can be found in Table 4. The sensitivity is specified as the registered counts for one second and one MBq of ^{57}Co. It can be seen that the sensitivity for the individual detectors vary up to a factor of 2 with the source position.

Table 4: The measured sensitivity as counts per second per MBq for a ^{57}Co spot marker placed at the focal point and 2 cm along each direction on the vertical, longitudinal and lateral axis.

	Source position						
Projection	**Focus**	**Anterior**	**Posterior**	**Cranial**	**Caudal**	**Sinister**	**Dexter**
1	14.8	17.1	14.5	14.0	13.6	14.3	18.6
2	42.0	56.1	30.2	48.1	37.5	40.5	44.4
3	28.9	39.7	29.3	34.5	28.5	37.6	28.6
4	24.9	14.9	25.0	23.2	20.4	29.7	17.0
5	14.4	13.7	14.6	13.3	11.1	18.5	11.7
6	15.6	18.1	16.1	8.04	17.3	14.1	20.1
7	31.9	39.7	26.7	31.2	28.5	24.6	36.3
8	52.9	73.8	39.8	53.0	50.1	45.9	58.2
9	46.2	68.7	39.7	48.8	49.6	54.6	41.9
10	40.0	33.1	30.7	39.7	39.3	45.3	15.8
11	23.7	33.5	32.3	26.6	26.2	39.1	19.8
12	26.5	17.6	31.2	24.3	23.8	34.9	16.9
13	19.9	20.3	19.1	19.0	20.3	25.7	16.4
14	13.8	12.2	15.9	13.6	12.4	17.0	11.6
15	11.2	16.5	14.2	13.4	15.9	13.3	18.5
16	41.6	55.4	34.3	33.6	46.8	39.8	45.3
17	38.3	35.8	30.7	30.8	6.80	39.2	23.5
18	17.6	14.6	24.5	18.0	20.55	27.3	10.5
19	11.2	13.0	14.9	11.1	12.17	15.5	10.8

The sensitivity in the reconstructed images was calculated as the sum of counts in the slices containing the point source for each measurement at seven positions within the FOV. The total pixel

values and the sensitivity relative to the focal point can be found in Table 5. The sensitivity variation in the reconstructed images is a few percent of the sensitivity variation for individual detectors when the spot marker changes position.

Table 5: The total pixel values and the relative sensitivity in the reconstructed images based on the measurement of a spot marker placed at seven different positions within the FOV. The distance between the measurement points was 2 cm.

Source position	Total pixel values	Relative sensitivity
Focus	$1.98\ 10^8$	1.00
Anterior	$1.93\ 10^8$	0.98
Posterior	$2.05\ 10^8$	1.04
Cranial	$1{,}98\ 10^8$	1.00
Caudal	$1{,}89\ 10^8$	0.96
Sinister	$2.02\ 10^8$	1.02
Dexter	$1.99\ 10^8$	1.01

The image dependence on the energy window

When the energy window in the measurement of a phantom with a myocardial defect was changed from ±10% to ±5% the mean counts in the heart ROI changed from 4957 to 3950, which means that 80% of the counts in the energy window ±10% is also within the energy window ±5%. In order to compensate for the loss of counts the acquisition has to be increased by 25%.

One of the horizontal long axis slices for ±10% and ±5% can be seen in Figure 14.

A 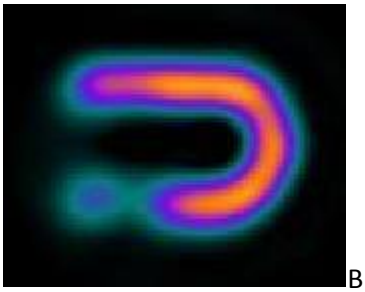 B 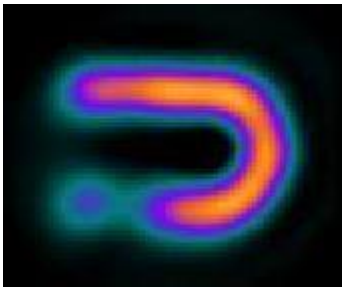

Figure 14: Horizontal long axis slice for ±10% energy window (A) and ±5% energy window (B) respectively.

As can be seen in Table 6 the contrast between the defect and the myocardium increases slightly. The change of a contrast of 0.02 is too small to be visible, as can been seen when comparing Figure 14A and B.

Table 6: Contrast between the defect and myocardium in the image from the phantom measurement with 10% and 5% energy window

Energy window [%]	Contrast
±10	0.60
±5	0.62

The scattered photons give rise to a halo around the heart (Figure 15). The intensity of the halo is greater for the energy window ±10% compared to the halo for the energy window ±5%. The halo is more noticeable with a change in windowing. The windowing levels are $1{,}3 \cdot 10^5$ (maximum), $4 \cdot 10^3$ and 10^3.

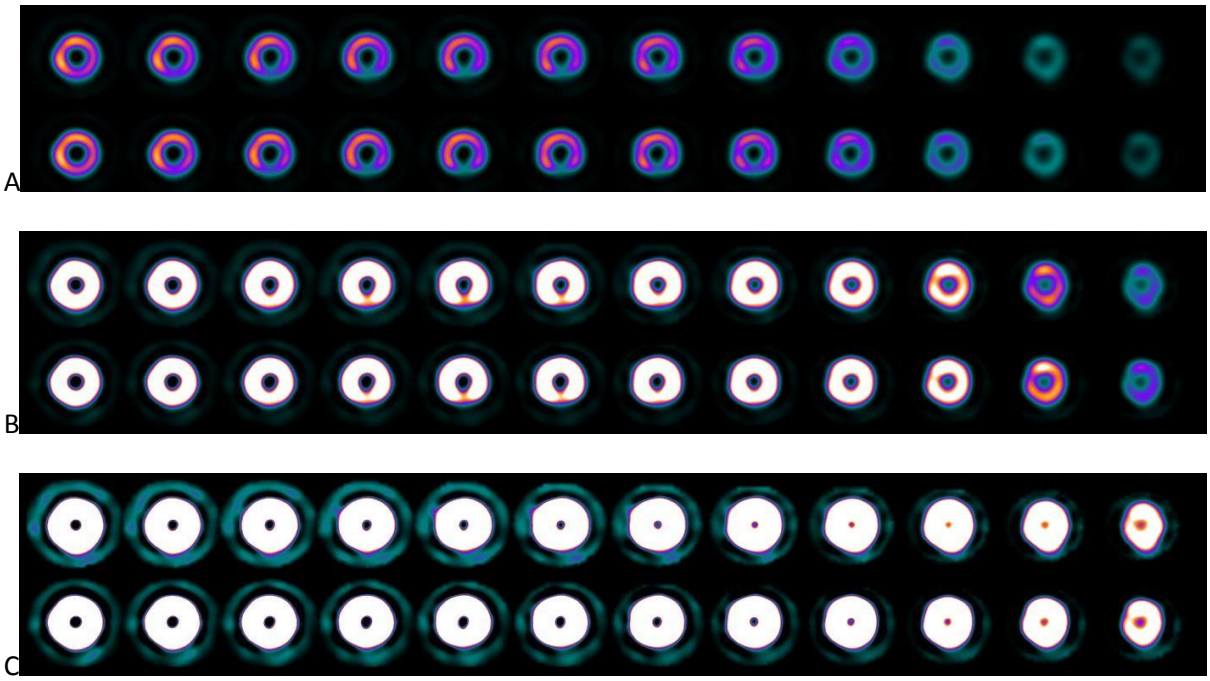

Figure 15: The short axis slices of the heart from the measured phantom with a windowing of $1{,}3 \cdot 10^5$ (maximum) (A), $4 \cdot 10^3$ (B) and 10^3 (C). The upper row the energy window of ±10% and lower row show the energy window ±5%.

The entire ventricle wall with energy window ±10% and ±5% and the subtraction between them can be seen as polar plots in Figure 16.

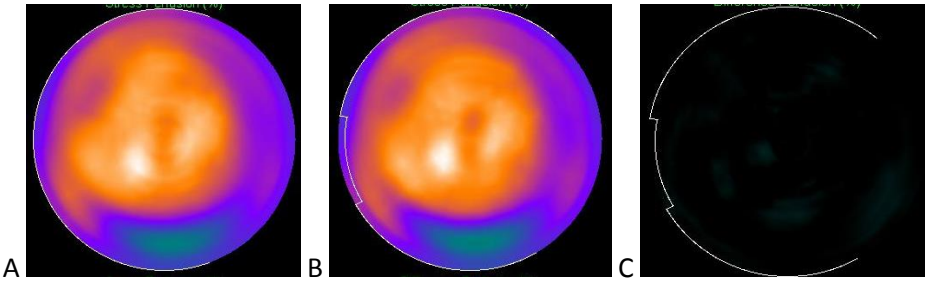

Figure 16: Polar plot for energy window ±10% (A) and ±5% (B) and the difference between them (C).

The image dependence on the reconstruction parameters

The result of a patient image when changing the number of MLEM iterations while having α, β and the post filtering fixed can be seen in Figure 17. The visual image quality is improved up to 60 iterations. When more iterations are performed the change in the image is a slight decrease in the minimum value in the ventricle, while the mean value remains constant. At more than 60 iterations unwanted hotspots start to appear.

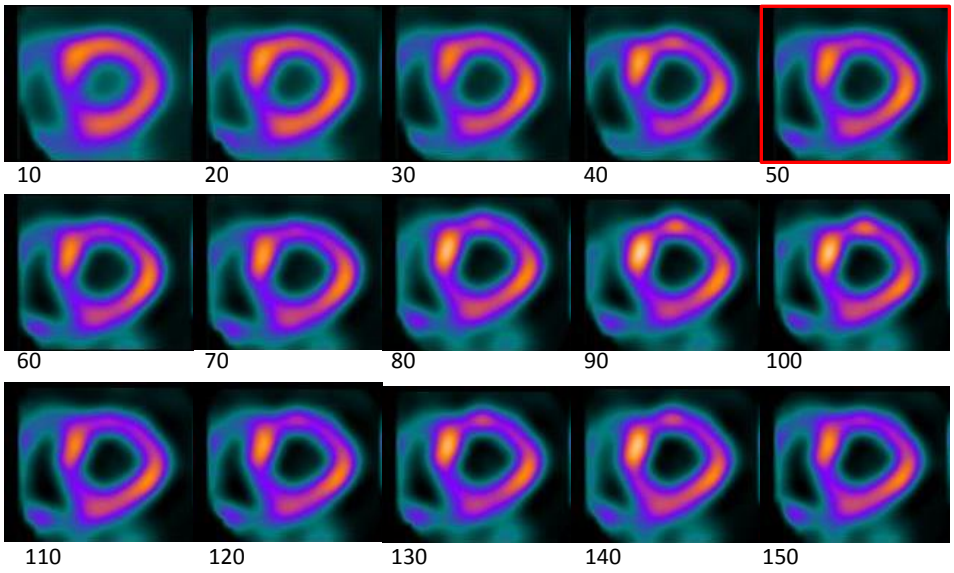

Figure 17: Short axis slice of a heart with the reconstruction parameters α and β as 0.41 and 0.20, the cut off frequency as 7 and the number of iterations ranging from 10 to 150. The clinically used settings are framed with red.

The results for different values of α and β with a fixed number of iterations and filter can be seen in Figure 18. The apparent myocardial thickness increases with an increasing αand β due to the smoothing effect. The effect on the image when changing β increases with an increasing α because α and β are multiplicative in the OSL correction. Note how the image for α 0.20 and α 0.80 changes when β changes from 0.10 to 0.50

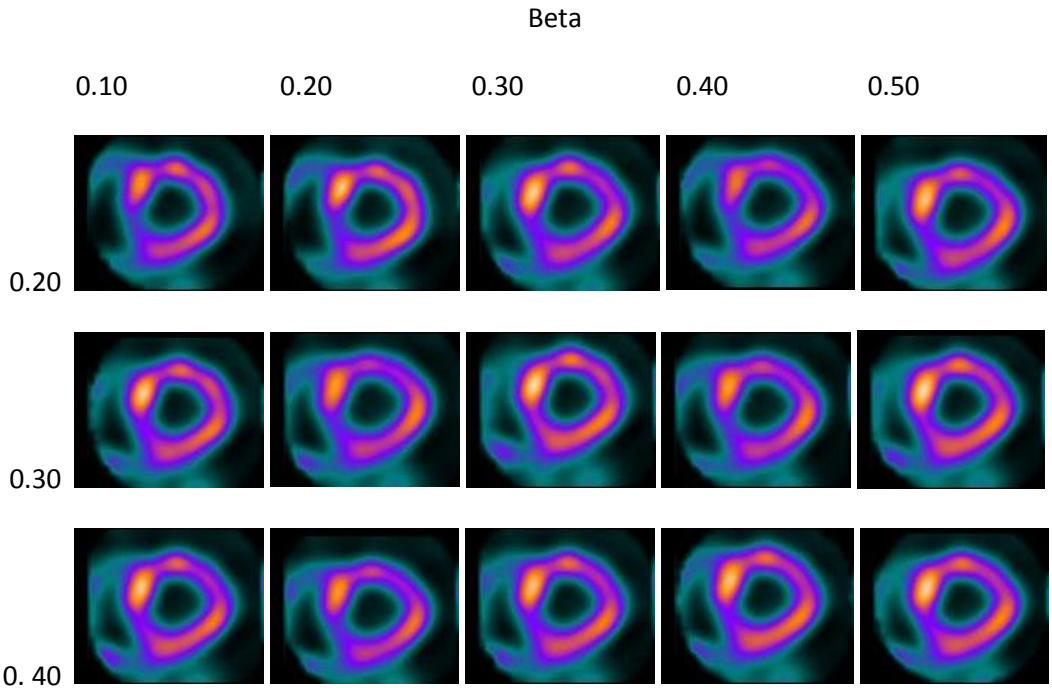

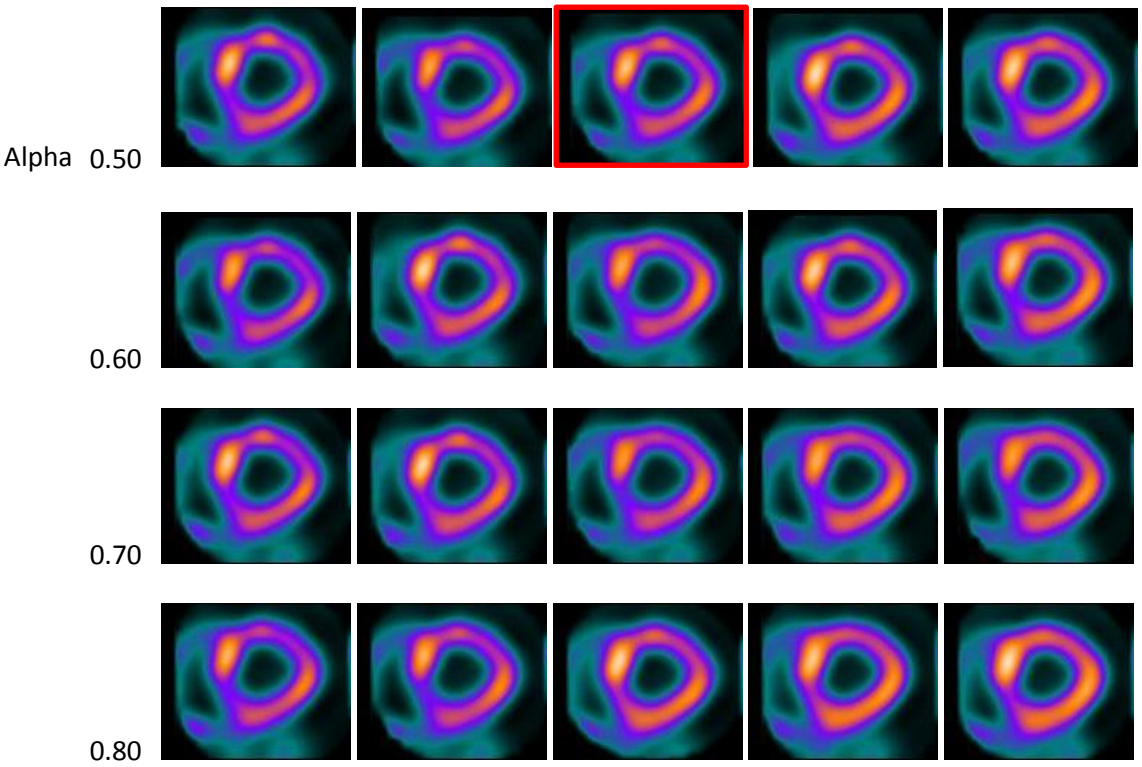

Figure 18: Short axis slice of a heart with the reconstruction parameters 40 iterations, cut off frequency 0.37, power 7 and a variable alpha and beta. The clinically used settings are framed with red.

The result for different cut off frequencies on the Butterworth filter can be seen in Figure 19. When the cut off frequency increases there is less smoothing of the image, the image noise is also increased.

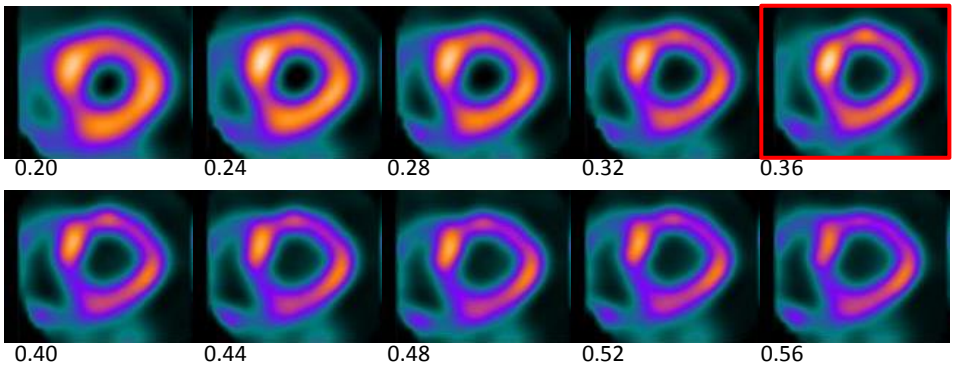

Figure 19: Short axis slice of a heart with the reconstruction parameters α and β as 0.41 and 0.2, 40 iterations, power 7 and the cut off frequency of the Butterworth filter ranging from 0.20 to 0.56. The clinically used settings are framed with red.

The chosen sets of reconstruction parameters slightly improved the contrast between the defect and the myocardium. When the sets were applied to the patient data and were presented to the physician there was no change in image quality. The conclusion was therefore that the currently used clinical reconstruction parameters were already optimized for the detection of lesions.

The image dependence on the source location

The dependence on the source location was evaluated with the heart phantom at different positions within the FOV. The mean pixel value in a ROI covering the heart in detector 8 for each of the phantom positions can be found in Table 7. Detector 8 had the most number of counts which led to

an optimal positioning of the ROI. The measurement in the focal point had twice as long acquisition time as the other measurement so the mean pixel value was halved before noted in the table. The mean pixel values were decay compensated for the time between the measurements but not compensated for decay during the acquisition.

Table 7: Mean counts for ROI over the heart in detector 8, corrected for different acquisition times and decay between the measurements, and the ventricle volume for phantom measurements at four locations within the FOV. The distance between focus point and the other points was 2 cm.

Position	Mean pixel value	Ventricle size [ml]
Focus	172	65
Posteror	173	64
Kranial	172	62
Kaudal	173	63

The polar plot for the focus position, the posterior position, the cranial position, the caudal position can be seen in Figure 20.

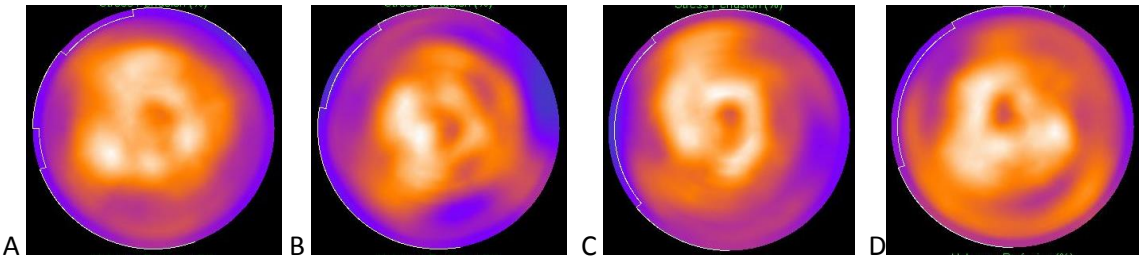

Figure 20: Polar plot for a heart phantom placed in the focal position (A), 2 cm posterior (B), 2 cm cranial (C), 2 cm caudal (D).

The polar plot for a patient in three different positions within the FOV can be seen in Figure 21.

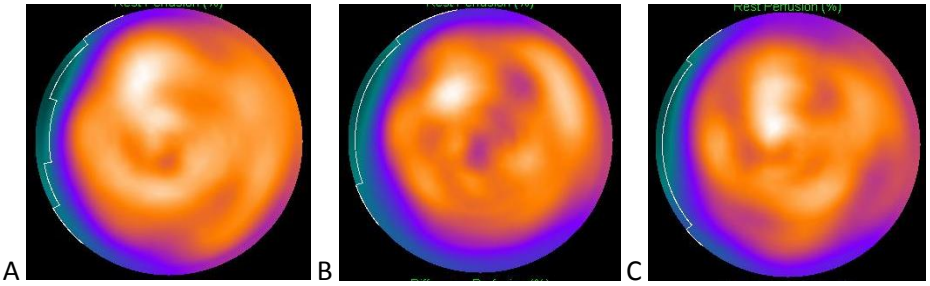

Figure 21: Polar plot for a patient placed in an optimal position (A), 2 cm posterior (B) and 2 cm cranial.

The detectability of small lesions

To find the detection limit for size of the heart defect, simulations were performed with defects covering different portions of the heart wall thickness and at different positions. The defect covered 60° and had a length of 2 cm. Simulation were performed on the virtual Data Spectrum phantom with a cardiac insert and on an XCAT phantom.

In the virtual Data Spectrum phantom the defects were 15%, 30% and 45% of the wall thickness placed anterior and inferior. For the anterior position the polar plots can be seen in Figure 22 and long axis slices at the defect can be seen in Figure 23. A physician determined that the defect of 15%

would not be classified as defect, but would be noted as a small change in the wall thickness. The defects with a thickness of 30% and 45% would be classified as a blood flow deficiency.

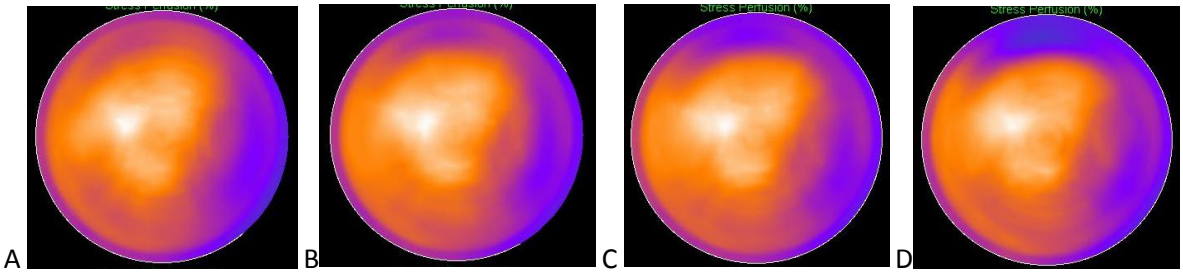

Figure 22: Simulation of a virtual Data Spectrum phantom with an anterior basal defect with a thickness of 0% (A), 15% (B), 30% (C) and 45% (D) of the myocardial wall.

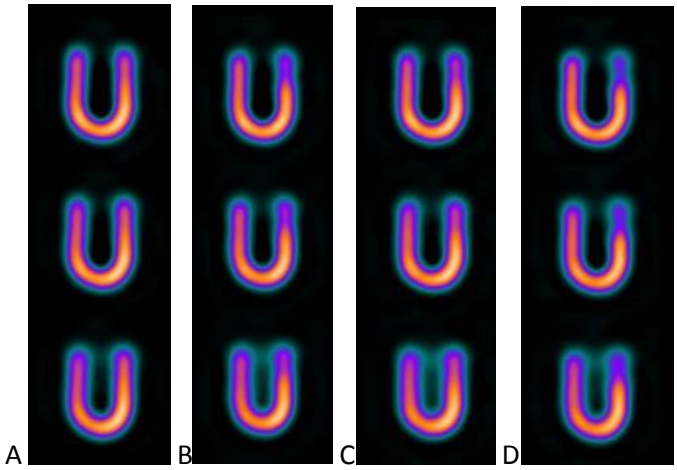

Figure 23: Rotated vertical long axis slices of a virtual Data Spectrum phantom with anterior heart defect with thickness 0% (A), 15% (B), 30% (C) and 45% (D) of the myocardial wall.

When the defects were placed in the inferior wall, the change in wall thickness is placed in an area where the attenuation is high. The physician determined that the defects of thickness 30% and 45% would be found and classified as a blood flow deficiency and the defect 15% would be noted as a small change, but would not be classified as a blood flow deficiency. The area with attenuation would appear more at the “six o’clock” position in the polar plot for a patient which could change the result. The polar plots and long axis slices can be seen in Figure 24 and Figure 25 respectively.

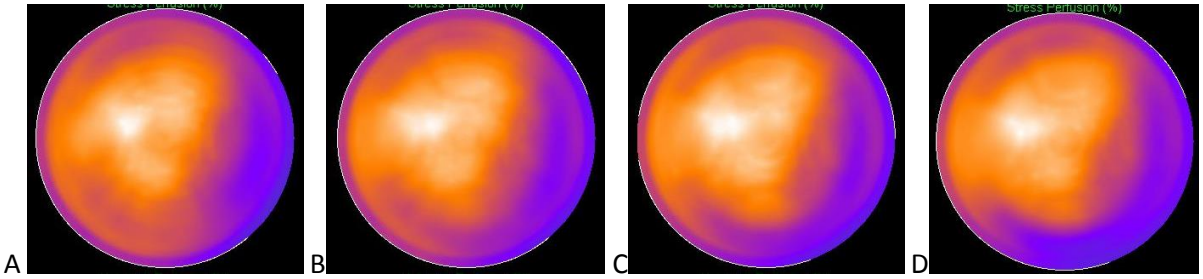

Figure 24: Simulation of a virtual Data Spectrum phantom with an inferior basal defect with a thickness of 0% (A), 15% (B), 30% (C) and 45% (D) of the myocardial wall.

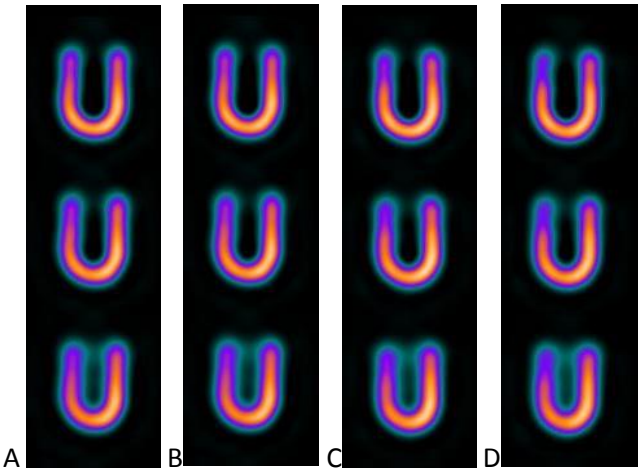

Figure 25: Rotated vertical long axis slices of a virtual Data Spectrum phantom with inferior heart defect with thickness 0% (A), 15% (B), 30% (C) and 45% (D) of the myocardial wall.

Simulation with the XCAT phantom with an anterior defect with a thickness of 0%, 15%, 30% and 45% of the heart wall were performed for the CZT camera. The resulting polar plots can be seen in Figure 26. There is a difference between the images that cannot be explained by the defect size. The unpredictable nature of the images makes it difficult to find the defect detection limit. Further work with the XCAT phantom is needed.

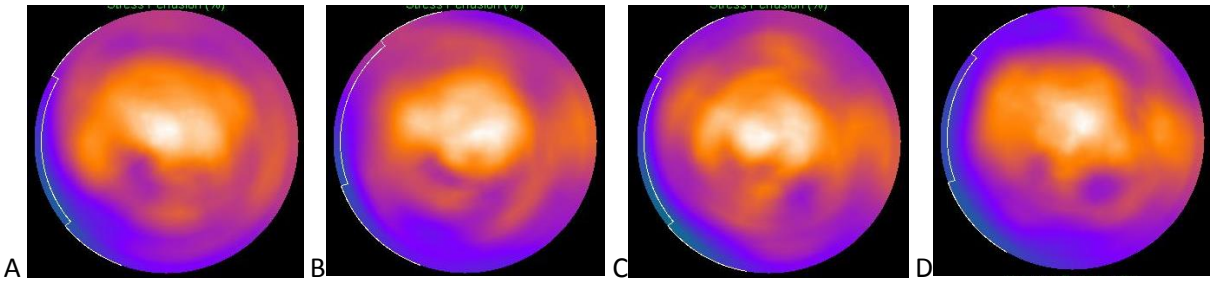

Figure 26: Polar plot for simulated XCAT phantom with an anterior basal defect with the thickness of 0% (A), 15% (B), 30% (C) and 45% (D) of the myocardial wall.

Comparison: CZT camera versus NaI(Tl) scintillation camera

Simulations of a Ventri acquisition of the virtual Data Spectrum phantom with a cardiac insert were performed with the SIMIND software. In the simulations inferior basal defects with a wall thickness of 15%, 30%, 45% and 100% respectively were used and one simulation was without defect. A vertical longs axis slice over the defect can be seen in Figure 27. The corresponding simulation with the Discovery NM 530c can be seen in Figure 28.

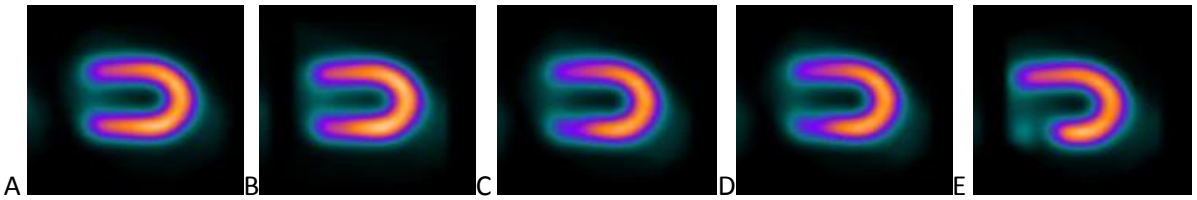

Figure 27: Vertical long axis slice from a simulation with the Ventri for a virtual Data Spectrum phantom without a defect (A), defect with 15% (B), 30% (C), 45% (D) and 100% (E) of the wall thickness. Slice thickness 6 mm.

Figure 28: Vertical long axis slice from a simulation with the Discovery NM 530c for a virtual Data Spectrum phantom without a defect (A), defect with 15% (B), 30% (C), 45% (D) and 100% (E) of the wall thickness. Slice thickness 4 mm.

Discussion

Monte Carlo verification

The spot marker is a cylinder with a diameter and height of 3.5 mm [16], which makes it too large to be considered a point source. Since the size and orientation of the source is known the source can be properly simulated and the size of the source is not an issue. According to the product information the inaccuracy in the spot markers activity is 15% [16]. This inaccuracy has greater impact on the total inaccuracy than any errors that come from couch movement or positioning on the grid paper, which is approximated to 1 mm, which only provides a slight inaccuracy. When comparing the simulated sensitivity to the measured sensitivity it is found to vary to the simulation had a 20% higher sensitivity. This difference was found to be acceptable. The comparison between the simulated and the measured images of the Data Spectrum phantom show that the simulation software produces acceptable images. The criteria which the images were compared with were the defect appearance and position, the attenuation effects and the heart volume. After the SIMIND software was verified it could be used in other parts of this work.

The spatial resolution

Since the spatial resolution of the reconstructed images is several mm the line source with an inner diameter of 0.6 mm and the one with 0.86 mm produced very similar results. Because difference in inner diameter does not affect the result the two measurements can be said to be on an identical source and therefore the second measurement is a replication of the first. The reconstructed pixel size is so large that the Gaussian fit is performed on three pixels which lead to a relatively poor fit. It is difficult to tell if the variation in the FWHM arise from an actual variation in the spatial resolution or from the few pixels. The positioning of the line source relative to the pixels highly influence the result, the line source can mainly be located in one pixel and therefore give rise to a sharp peak or it can be positioned in the intersection between two pixels and rive rise to a partial volume effect.

It should be noted that the measurement points are not equidistant. The distance between the measurement points on a single line is approximately 8 cm apart while the distance to the central point is 2 cm when comparing the resolution within the cranial, central and caudal groups. The results show that the spatial resolution does not vary noticeably within the measured area and that the differences may come from the fitting problems stated earlier.

The sensitivity

It has been shown that the sensitivity for the individual detectors varies with the source position. Theoretically the sensitivity increases when the source is moved closer to the pinhole. When the source is moved parallel to the detector the projection changes position in the detector and the sensitivity is constant. It is of importance to know where each of the detectors is located in order to fully be able to evaluate the result. The exact location of the detectors and the angle of the pinhole collimators are not public information but there is an approximate position known for each detector. With the camera position at the measurement detector 1, 2, 6, 7, 8, 15 and 16 got a top down view, detector 4, 5, 12, 13, 15 18 and 19 got a side view and detector 3, 6, 10, 11 and 17 view the source at~45°.

It is also of importance to see if the sensitivity in the reconstructed images changes with the source position or if the change in sensitivity and the projection positions for the different detectors compensate each other. The variation in the sensitivity in the reconstructed images was 4%. It should be noted that the measurements were 2 cm apart from each other and the sensitivity would probably start to decrease as the distance to the focal point increased.

The image dependence on the energy window

As shown in Table 6, the contrast between the defect and the myocardium is only slightly changed when the energy window is reduced. This change in contrast is not noticeable by eye. The scattered radiation that is within the energy window leads to a mispositioning of events. The mispositioning can lead to that the activity in the cavity and the activity outside the heart is increased, this reduces the contrast between the heart and the cavity. As can be seen in Figure 15 the scattered radiation results in a halo around the heart after the reconstruction. The halo is more visible with a reduction in the range of the color look up table. When the energy window is changed from ±10% to ±5% the halo is reduced in width and intensity. The halo is not visible in patient imaging due to the background activity. The reduction in the halo size with the change in energy window does not affect the polar plot in any noticeable way. The effect of reduced scattering is expected to be seen around the defect and the edge of the polar plot in the difference between the plots, Figure 16C. The difference plot shows that there is little or no difference between the two energy window settings.

Since there are only subtle changes in the reconstructed image it can be deduced that the low-energy tail in the spectrum mainly contain registered events which have lost energy due to trapping, recombination or charge sharing, all which are correctly positioned. The aim of changing the energy window is to improve image quality by removing scattered events in the low energy tail. However the result is a reduced signal to noise ratio due to the reduced statistics but with no changes to the image contrast. In order to achieve the same amount of counts as with an energy window of ±10% the acquisition time or injected activity must be increased by 25%.

The image dependence on the reconstruction parameters

When studying the effects on images for different number of iterations it can be seen that the image converges rapidly and that there is only small changes after 40 iterations. The changes after 40 iterations are mainly the activity within the cavity, which results in a higher contrast between the cavity and the myocardium. The contrast change however is too small to be seen by eye. The increase in the noise level at high number of iterations is canceled out by the post reconstruction filtration. If one wish to study the MLEM reconstruction more in depth the same investigation could be made without any post reconstruction filtering. Since post filtering will always be applied in clinical applications this work has been limited to post filtered images. The OSL regularization is applied between each MLEM iteration and got two user specified variables, α and β. While it acts in the spatial domain it does not smooth the image like the Butterworth filtration. The Butterworth post reconstruction filter is a low pass filter for spatial frequencies. The filter basically smears or smooth out the counts. When studying the images in Figure 19 it appears as if there are more counts in the images with low cut off frequency, this is false. Each image utilizes a relative color scheme which is fitted to the maximum value in each image. When the post reconstruction is applied the maximum value gets closer to the mean value. When the cut off frequency is low a large portion of the myocardium gets similar values and intensity close to the maximal value. When the cut of frequency is increased the noise level and the contrast between the myocardium and the cavity increases. When the cut of frequency has been increased to a certain point there are only changes which are too small to the affect the visual appearance of the image. Changing the power of the Butterworth filter has a negligible effect on the final image unless it is reduced to the lowest power i.e. 1.

The image dependence on the source location

Due to the geometry of the phantom it was not possible to place the heart completely in the focal point, the distance between the preferred and actual position was about 1 cm. The difficulties of placing the phantom at the correct initial position cause the comparison with the other positions to not be made with the actual focal point. When a comparison of mean count for the different positions was made it was found to be a perfect match for all phantom positions.

The evaluation software uses auto segmentation of the myocardial wall and the segmentation gives the boundaries for the polar plot and is used directly to calculate the ventricle volume. There is a slight difference in the segmentation near the heart base for each position for each position. The difference leads to that the ventricle volume is between 62 and 65 ml, depending on the position, while the actual ventricle volume is $\sim$60ml according to the phantom manufacturer. This means that there is an approximate uncertainty in the determination of the ventricle volume is about 8%. The base of the heart is located at the edges of the polar plot and the generous segmentation can be seen as a blue, low activity, outline at the edges and this should not affect the rest of the plot.

The reconstructed activity distribution changes with the phantom position, as seen in Figure 20. The ideal situation is that the uniformity achieved at the focal point remains at the other positions. The mean counts in the projection directly above the focal point does not change with the phantom position, but since pinhole collimators are used the minification factor and the projection location changes when the phantom is moved away from the focal point. The change to each of the 19 projections is different for each translation and the reconstruction algorithm does not compensate for this since it is assumed that the object is placed in the focal point.

It is clear that a translation of 2 cm of the phantom affects the image of the activity distribution. It has been determined that the spatial resolution is uniform within the central portion of the field of view. The sensitivity has been found to vary greatly with the position for each of the detectors when measured with a spot marker; however the reconstructed sensitivity only varies 4% with the position. When the sensitivity is measured with the phantom it is found to be almost equal for all the positions. The spatial variation in sensitivity found when measured with the spot marker is averaged out because of the heart size. The explanation for this is that the heart is several cm along the short and the long axis and different parts of the heart is therefore projected differently on each of the detector panels, for example the anterior wall is enlarged compared to the inferior wall, but since the heart is super positioned projected in the detector this is not noticeable in the projection. A similar relation occurs for all the detector panels, but since panels only covers a part of the angles there is no symmetry around the heart. When a translation is performed different parts of the heart gets closer to the focus point while other parts are further away.

The phantom measurement was performed to study the positioning effects when all parameters were known. There are numerous image degradation effects when the camera is used in a clinical situation such as cardiac motion, respiratory movement, non-uniform activity distribution and background activity. It could possible that all these effects have a greater impact on the image than the positioning. The patient images show that even with all the above mentioned effect there is still a distortion of the image when the patient is moved 2 cm. It would have been inadequate to only investigate the positioning effects in a clinical setting because there would be no way to guarantee that the position was the only parameter changed between the measurements.

If the image distortion was predictable for a certain mispositioning the physicians would be able to tell a distortion apart from a blood flow deficiency. Insufficient data was gathered to investigate this in this work. The clinical routine at this point is to evaluate the acquired images before sending each patient home so that if a patient had been sub-optimally placed another acquisition could be performed without the need for another injection with radiopharmaceutical, which would lead to an increased dose. The avoidance of an image distortion is always better than compensation, but the predictability would still be of interest in cases where the positioning still was wrong.

The detectability of small lesions

Because the position and the angle of the heart in the Data Spectrum phantom differs from that of a patient the attenuation is different from the attenuation in a patient. The attenuation effect was verified to be in the correct area by a comparison with the measurement. The choice of heart angle in the Data Spectrum phantom is limited when the lung insert is used and the digital phantom used for the simulation is based on the physical phantom. The inferior defects are not placed in the middle of the attenuation region, but close enough that the contrast is reduced. When using the Data Spectrum phantom the detection limit for a 2 cm high 60° defect placed near the base of the heart is somewhere between 15% and 30%. It has been found that there are difficulties detecting defects that is less than 50% of the heart wall [20].

When the simulation was performed with the XCAT phantom an anterior basal attenuation effect was discovered that are not present in most patients. This attenuation comes from the positioning of the heart in phantom and it is difficult to change. When the simulation results were compared for different heart defects it was found that there were changes is areas without any defect. It is difficult

to find an explanation for this without deeper knowledge about SIMIND and XCAT. The simulated images produced by SIMIND for the XCAT phantom cannot be used to find the detection limit for the defects at this time. However, if the images were more predictable it would be possible to find the limit for the XCAT phantom and determine if the cardiac movement changes the detection limit.

Comparison: CZT camera versus NaI(Tl) scintillation camera

When the slices from the simulation of the Ventri system and the Discovery NM 530c system are compared it is clear that CZT camera produces images with superior quality. There are less thickening of the ventricle wall and a more accurate visualization of the defect for the Discovery camera. Because of the improved spatial resolution the heart wall is thinner in the CZT images and the ventricle appears to have a lower activity concentration. The images produced with the NaI(Tl) camera is noisier, but that might be a result of a softer post processing filter. More filtration would also push the activity into the ventricle. The defects are clearer with the CZT camera due to a lesser degree of partial volume effects. It should be noted that most physicians are used to the images produced with NaI(Tl) cameras and physicians need to practice with the CZT images to get accustomed to them.

Conclusions

The SIMIND software was verified for the Discovery NM 530c by comparing measurement and simulation of a spot marker and a Data Spectrum phantom with a cardiac insert with a basal defect. The spatial resolution was found not to vary within the investigated area. The detector specific sensitivity varies greatly with the source position, but the sensitivity obtained from the reconstructed images only varies 4%. The uniform sensitivity shows that the reconstruction algorithm is insensitive to detector specific variations. While the spatial resolution and the reconstructed sensitivity varies less than 4% in a volume close to the focus the image dependence on the source position that might affect the diagnosis with a translation of 2 cm. Insufficient data were gathered to see a significant predictability in the image change for the translation directions. Attempts to improve the contrast between a myocardial defect and the healthy myocardium were made by changing the reconstruction parameters. No improvement in contrast could found so the reconstruction parameters were optimized for the acquisition protocol. The detection limit for a basal, 2 cm high, 60° myocardial defect was found to be between 15% and 30% of the wall thickness for the virtual Data Spectrum phantom. The defects placed anterior were easier to identify than the inferior defects. The detection limit was not found for the XCAT phantom because of difficulties with the image evaluation.

Acknowledgements

The author would like to thank Fredrik Hedeer M.D. for image evaluation and valuable insights and Christel Kullberg, biomedical technician, for technical expertise.

Appendix 1

The trapping and recombination of holes is a random process which makes it difficult to determine the fraction of charges lost for each interaction depth. The induced charge as a function of interaction depth can be approximated with several models. One of these models results in the Hecht equation, Equation 4 [8]. The Hecht equation gives the induced charge as a function of the detectors thickness, the average energy required to create an electron-hole pair and the mean free paths of the electrons and holes.

Equation 4

$$Q(z) = \frac{E}{w} e \left(\frac{\lambda_e}{d}\right)\left(1 - e^{(d-z)/\lambda_e}\right) + \left(\frac{\lambda_h}{d}\right)\left(1 - e^{-z/\lambda_h}\right)$$

Where Q(z) is the induced charge, E the deposited energy, w the average ionization energy which is about 4.6 eV for CZT, e = 6 x 10^{-19} C, d the crystal thickness, z the depth into the crystal from the cathode front surface, and λ_e and λ_h are the mean free paths of electron and holes respectively.

References

1. Wagenaar, D.J., *CdTe and CdZnTe Semiconductor Detectors for Nuclear Medicine Imaging*, in *Emission Tomography: The fundamentals of PET and SPECT*, M. Wernick and J. Aarsvold, Editors. 2004, Elsevier Inc. p. 270-292.
2. Bocher, M., et al., *A fast cardiac gamma camera with dynamic SPECT capabilities: design, system validation and future potential.* Eur J Nucl Med Mol Imaging, 2010. **37**(10): p. 1887-902.
3. Buechel, R.R., et al., *Ultrafast nuclear myocardial perfusion imaging on a new gamma camera with semiconductor detector technique: first clinical validation.* Eur J Nucl Med Mol Imaging, 2010. **37**(4): p. 773-8.
4. Mouden, M., et al., *Impact of a new ultrafast CZT SPECT camera for myocardial perfusion imaging: fewer equivocal results and lower radiation dose.* Eur J Nucl Med Mol Imaging, 2012. **39**: p. 1048–1055.
5. Gengsheng, L., *Single-Photon Emission Computed Tomography*, in *Emission Tomography*, M. Wernick and J. Aarsvold, Editors. 2004, Elsevier Inc. p. 127-154.
6. Knoll, G.F., *Radiation detection and measurement*. 3. ed. 2000, New York ; Chichester: John Wiley. xiv, 802 s.
7. Levin, C., *Application-Specific Small Field-of-View Nuclear Emission Imagers in Medicine*, in *Emission Tomography: The fundamentals of PET and SPECT*, M. Wernick and J. Aarsvold, Editors. 2004, Elsevier Inc. p. 292-332.
8. Chen, L. and Y.X. Wei, *Monte Carlo simulations of the SNM spectra for CZT and NaI spectrometers.* Appl Radiat Isot, 2008. **66**(8): p. 1146-50.
9. Iniewski, K., et al., *Modeling Charge-Sharing Effects in Pixellated CZT Detectors*, in *2007 IEEE Nuclear Science Symposium Conference*2007.
10. GE, *Alcyone Technology White Paper*.
11. Herzog, B.A., et al., *Nuclear myocardial perfusion imaging with a cadmium-zinc-telluride detector technique: optimized protocol for scan time reduction.* J Nucl Med, 2010. **51**(1): p. 46-51.
12. Guerra, P., A. Santos, and D.G. Darambara, *Development of a simplified simulation model for performance characterization of a pixellated CdZnTe multimodality imaging system.* Phys Med Biol, 2008. **53**(4): p. 1099-113.
13. Oddstig, J., et al., *Reduced administered activity, reduced acquisition time, and preserved image quality for the new CZT camera.* Journal of nuclear cardiology, 2012. **Volume 20**(Issue 1): p. 38-44.
14. Green, P.J., *Bayesian Reconstructions From Emission Tomography Data Using a Modified EM Algorithm.* IEEE TRANSACTIONS ON MEDICAL IMAGING, 1990. **9**(1): p. 84-93.
15. Lalush, D.S. and M.N. Wernick, *Iterative Image Reconstruction*, in *Emission tomography*, M.N. Wernick and J.N. Aarsvold, Editors. 2004, Elseveir Inc. p. 443-472.
16. *Medical Imaging Sources Product Information*, Eckert & Ziegler Isotope Products.
17. Ljungberg, M., *The SIMIND Monte Carlo Program*, in *Monte Carlo calculations in nuclear medicine*, M. Ljungberg, S.-E. Strand, and M. King, Editors. 2012. p. 111-128.
18. Zubal, G. and P. Segars, *Anthropomorphic Phantoms: Early Developments and Current Advancements*, in *Monte Carlo calculations in nuclear medicine*, M. Ljungberg, S.-E. Strand, and M. King, Editors. 2012. p. 31-44.
19. Soneson, H., *Methods for quantitative analysis of myocardial perfusion SPECT : validated with magnetic resonance imaging, phantom studies and expert readers*, 2012: Centre for Mathematical Sciences, Lund University
20. Wagner, A., et al., *Contrast-enhanced MRI and routine single photon emission computed tomography (SPECT) perfusion imaging for detection of subendocardial myocardial infarcts: an imaging study.* The Lancet, 2003. **Vol 361**: p. 374-79.